EurJIC European Journal of Inorganic Chemistry

ChemPubSoc Europe

SHORT COMMUNICATION

DOI:10.1002/ejic.201301307

Thermal Conversion of Hollow Prussian Blue Nanoparticles into Nanoporous Iron Oxides with Crystallized Hematite Phase

Mohamed B. Zakaria,[a,b,c][‡] Ming Hu,[b][‡] Naoaki Hayashi,[d] Yoshihiro Tsujimoto,[e] Shinsuke Ishihara,[b,f] Masataka Imura,[b] Norihiro Suzuki,[f] Yu-Yuan Huang,[g] Yoshio Sakka,[e] Katsuhiko Ariga,[b] Kevin C.-W. Wu,[g] and Yusuke Yamauchi*[a,b,h]

Keywords: Mesoporous materials / Nanoparticles / Nanoporous materials / Iron / Prussian blue

We recently demonstrated that Prussian blue (PB) coordination polymers can be successfully etched by acidic solution for the preparation of hollow PB nanoparticles (*Angew. Chem. Int. Ed.* **2012**, *51*, 984). In this paper, by using hollow PB nanoparticles as starting materials, we calcined them under various conditions to prepare nanoporous Fe oxides with a crystallized α-Fe_2O_3 (hematite) phase. The obtained particles were carefully characterized by scanning electron microscopy, wide-angle X-ray diffraction, nitrogen gas adsorption–desorption isotherms, transmission electron microscopy, and Mössbauer spectroscopy. The morphologies, surface areas, and degrees of crystallinity of the samples were varied by changing the number of hours of calcination. After calcination at 400 °C for 4 h, formation of a crystallized α-Fe_2O_3 phase was confirmed, although some residues of amorphous and/or γ-Fe_2O_3 phases were also present. With a further increase in the calcination time (up to 7 h), the α-Fe_2O_3 phase was predominantly formed. The obtained sample exhibited high surface area, which will be useful for photocatalytic applications.

Introduction

Various inorganic nanoporous materials have been drawing intense research interest not only for their unique structural, optical, and surface properties, but also for their broad range of applications, which include their use in catalysis, drug delivery, and chemical storage. Among these materials, iron oxides are potentially useful for catalysts[1] and lithium-ion batteries.[2] Iron oxides can exhibit several crystal structures, including wüstite (FeO), magnetite (Fe_3O_4), maghemite (γ-Fe_2O_3), cubic (β-Fe_2O_3), hematite (α-Fe_2O_3), and orthorhombic (ε-Fe_2O_3). In particular, the interest in hematite (α-Fe_2O_3) has recently increased owing to its unique optical and magnetic behavior, high catalytic activity, suitable band gap, and low toxicity.

Developing new routes for the preparation of nanoporous α-Fe_2O_3 and investigating its distinct properties are of considerable interest. In a recent study, α-Fe_2O_3 hollow spheres with sheetlike subunits were synthesized by a facile quasiemulsion-templated method, in which glycerol was dispersed in water to form oil-in-water quasiemulsion microdroplets.[3] Porous α-Fe_2O_3 nanorods with diameters of 30–60 nm were also synthesized through thermal decomposition of $FeC_2O_4 \cdot 2H_2O$ nanorods prepared by a poly(vinyl alcohol)-assisted precipitation process. Compared to commercial submicrometer-sized α-Fe_2O_3 powders, porous α-Fe_2O_3 nanorods exhibit significantly enhanced capability as an electrode material for lithium-ion batteries.[4] As another example, 3D flowerlike iron oxide showed excellent ability to remove heavy-metal ions and other pollutants in water treatment.[5] Thus, nanoporous α-Fe_2O_3 materials with high surface areas have exhibited very interesting properties that

[a] Faculty of Science and Engineering, Waseda University, 3-4-1 Okubo, Shinjuku, Tokyo 169-8555, Japan
[b] World Premier International (WPI) Research Center for Materials Nanoarchitechtonics (MANA), National Institute for Materials Science (NIMS), 1-1 Namiki, Tsukuba, Ibaraki 305-0044, Japan
E-mail: Yamauchi.Yusuke@nims.go.jp
http://www.yamauchi-labo.com
[c] Department of Chemistry, Faculty of Science, Tanta University, Tanta, Gharbeya 31527, Egypt
[d] Institute for Integrated Cell-Material Sciences, Kyoto University, Yoshida-Ushinomiya, Sakyo, Kyoto 606-8501, Japan
[e] Materials Processing Unit, National Institute for Materials Science (NIMS), 1-2-1 Sengen, Tsukuba, Ibaraki 305-0047, Japan
[f] International Center for Young Scientists (ICYS), National Institute for Materials Science (NIMS), 1-2-1 Sengen, Tsukuba, Ibaraki 305-0047, Japan
[g] Department of Chemical Engineering, National Taiwan University, No. 1, Sec. 4, Roosevelt Road, Taipei 10617, Taiwan
[h] Precursory Research for Embryonic Science and Technology (PRESTO), Japan Science and Technology Agency (JST), 2-1 Hirosawa, Wako, Saitama 351-0198, Japan
[‡] These authors contributed equally to this work.
Supporting information for this article is available on the WWW under http://dx.doi.org/10.1002/ejic.201301307

Table 1. Summary of nanostructured α-Fe_2O_3 materials previously reported.

Shape	Fe source	Surface area [$m^2 g^{-1}$]	Ref.
Hollow spheres	$FeSO_4 \cdot 7H_2O$	103	[3]
Porous nanorods	$FeC_2O_4 \cdot 2H_2O$	11.8	[4]
3D flowerlike	$FeCl_3 \cdot 6H_2O$	40.0	[5]
Porous nanorods	$FeCl_3 \cdot 6H_2O$	–	[6]
Spherical nanoparticles	$FeC_2O_4 \cdot 2H_2O$	–	[7]
Mesoporous films	$FeCl_3$	–	[8]
Flutelike porous nanorods	β-FeOOH	125	[9]
3D urchinlike superstructures	$FeSO_4 \cdot 7H_2O$	86.8	[10]
Mesoporous nanorods	$Fe(NO_3)_3 \cdot 9H_2O$	105	[11]
Mesoporous nanorods	α-FeC_2O_4	125	[12]
Porous nanoparticles	$FeCl_3$	22.3	[13]
Porous nanorods	$FeCl_3 \cdot 6H_2O$	82.6	[14]
Spindlelike nanostructures	$Fe(NO_3)_3 \cdot 9H_2O$	66.8	[14]
Mesoporous thin films	$Fe(NO_3)_3 \cdot 9H_2O$	190	[15]
Mesoporous nanospheres	$FeCl_3$	18.2	[16]
Hollow-structured particles	$FeCl_3 \cdot 6H_2O$	–	[17]
Nanotubes	$Fe(NO_3)_3 \cdot 9H_2O$	–	[18]
Hollow microspheres	$FeCl_3 \cdot 7H_2O$	–	[19]
Hollow spheres	ferric potassium oxalate	41.1	[20]
Mesoporous particles	$FeCl_3$	335	[21]

are not attainable by bulk α-Fe_2O_3 without nanopores. Table 1 summarizes the structural parameters of various nanoporous α-Fe_2O_3 previously reported.[6–21]

Recently, we demonstrated the synthesis of hollow Prussian blue (PB) coordination polymers by chemical etching[22] and reported their thermal conversion into nanoporous iron oxide particles.[23] PB coordination polymers in which iron ions are bridged by cyano groups (–Fe^{II}–CN–Fe^{III}–) are considered potential precursors to nanoporous iron oxides with high surface areas, because the iron component can be oxidized and the organic components can be removed by calcination in air. This approach is simple and convenient, which is useful for the further preparation of several iron oxides with different degrees of crystallinity and different structures. Herein, we extend this concept to synthesize nanoporous iron oxides with the α-Fe_2O_3 phase. The obtained samples were carefully characterized by scanning electron microscopy (SEM), wide-angle X-ray diffraction (XRD), nitrogen gas adsorption–desorption isotherms, transmission electron microscopy (TEM), and Mössbauer spectroscopy.

Results and Discussion

For the creation of the hollow cavity, the synthesized PB particles (Figure 1, a) were treated with 1.0 M HCl solution in the presence of polyvinylpyrrolidone (PVP). The PVP polymer was on the external surface of the PB particles and thus could serve as a protecting agent during the HCl etching process.[22] Even after etching, the average diameter of the PB particles did not change (ca. 100 nm), and the corresponding particle size distribution was very narrow, as shown in Figure 1 (b). The diameter of the internal cavity was calculated to be approximately 80 nm. To prepare nanoporous iron oxides with hematite (α-Fe_2O_3) phase, we further calcined the hollow PB particles at 400 °C for different time durations (4, 5, 6, and 7 h). The samples were heated inside an electric furnace from room temperature to 400 °C at a heating rate of 1 °C min^{-1}. After that, the powder was cooled inside the furnace. Finally, the obtained powders were collected for further characterization. The entire calcination process was performed in air.

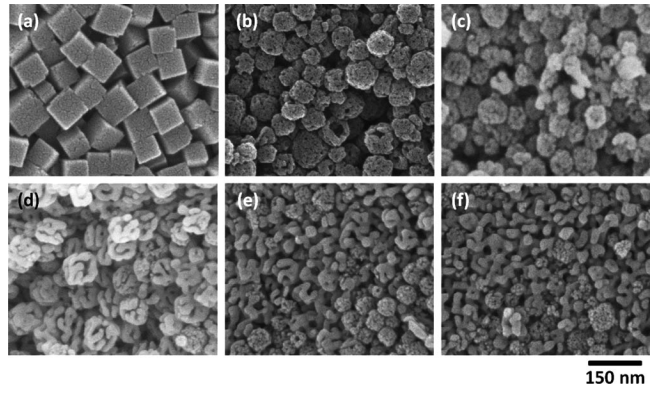

Figure 1. SEM images of (a) PB nanoparticles before chemical etching, (b) PB nanoparticles after chemical etching, and samples calcined for (c) 4, (d) 5, (e) 6, and (f) 7 h.

The morphology of the calcined samples was observed by scanning electron microscopy (SEM), as shown in Figure 1 (c–f). After calcination at 400 °C for 5 h, the surface structure of the hollow particles clearly changed as a result of the crystallization of the PB shell to iron oxide (Figure 1, d). With a further increase in the calcination time to 6 and 7 h (Figure 1, e,f), the hollow structure completely collapsed. In the starting PB crystals, the Fe atoms were stabilized by cyano bridges. Upon calcination at high temperatures under air flow, the C–N bridges were removed to form Fe oxides. After calcination, no carbon content was confirmed in the final product. The result of thermogravimetry/differential thermal analysis/mass spectrometry (TG–DTA–

MS) under He/O_2 flow (volume ratio = 80:20, flow rate = 200 mL min^{-1}) indicated several exothermic peaks at approximately 260–310 and 470 °C, accompanied with the production of CO_2 and/or N_2O (m/z = 44) as well as N_2 and/or CO (m/z = 28), which is typical for the combustion reaction of a CN-containing material. Emission of adsorbed H_2O (m/z = 18) was also detected. Molecules with masses larger than m/z = 50 were not detected by TG–DTA–MS up to 1000 °C.

To investigate the effect of the calcination time on the crystalline phases and degrees, we performed wide-angle XRD measurements, as shown in Figure 2. With an increase in the calcination time, the intensities of the peaks for the α-Fe_2O_3 phase gradually increased, which is indicative of an enhancement in crystal growth. The crystalline sizes were calculated by using the Scherrer equation. The average sizes varied from approximately 12.2 (for 4 h), 15.4 (for 5 h), and 17.1 nm (for 6 h) to 17.1 nm (for 7 h). Thus, the increase in the calcination time promoted the crystallization of α-Fe_2O_3, which thereby led to a collapse of the original hollow structure. As clearly seen in Figure 1 (e,f), the formation of large-sized nanopores was caused by the gradual crystallization of iron oxides.

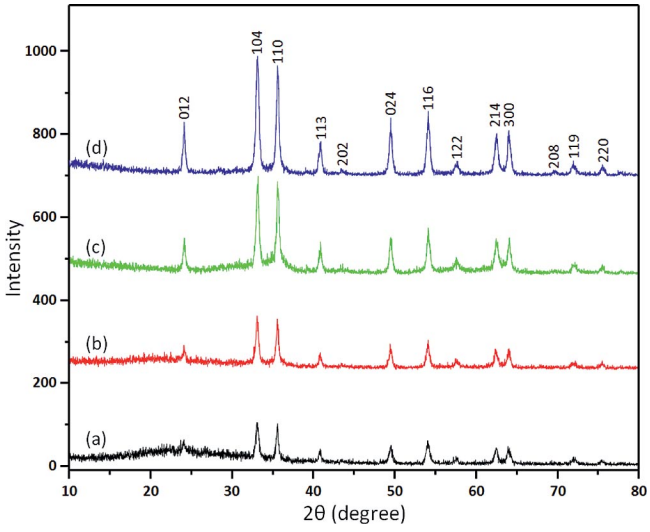

Figure 2. Wide-angle XRD profiles for samples calcined for (a) 4, (b) 5, (c) 6, and (d) 7 h.

To further understand the crystalline structure, we collected ^{57}Fe Mössbauer spectra from the calcined PB samples for 5 and 7 h, as shown in Figure 3. The spectroscopic data was well resolved into a sextet and a doublet with a peak/area ratio of 30:70. On the basis of the obtained Mössbauer parameters listed in Table 2, the former was assigned as α-Fe_2O_3. The latter exhibits an isomer shift characteristic of Fe^{III}, which was caused by the presence of impurities such as amorphous iron oxide and/or γ-Fe_2O_3 phases. Increasing the calcination time up to 7 h significantly improved the quality and volume fraction of α-Fe_2O_3 to around 65% (Table 2 and Figure 3, b). This is in good agreement with the XRD data above (Figure 2).

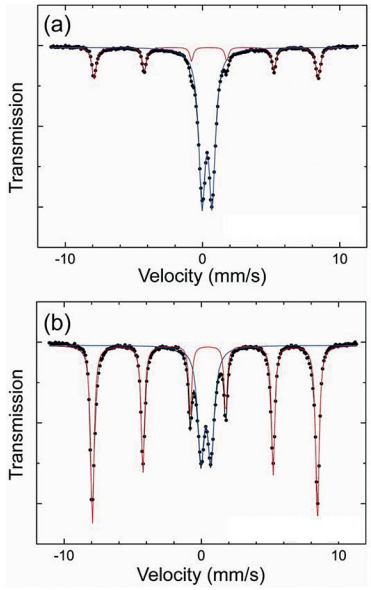

Figure 3. ^{57}Fe Mössbauer spectra collected at room temperature from samples calcined for (a) 5 and (b) 7 h. Red and blue lines represent the contributions from α-Fe_2O_3 and some impurity phases (amorphous and/or γ-Fe_2O_3).

The hollow structure of the starting hollow PB particles and the crystalline structure of the calcined iron oxide samples were examined by TEM, as shown in Figure 4. Solid PB nanocubes were transformed into hollow cubes after chemical etching (Figure 4, a). The sample that was calcined for 5 h showed morphology that was similar to that of the original hollow PB particles with similar particle sizes (Figure 4, b). The hollow structure was well retained even after the crystallization of the iron oxides. Selected-area electron diffraction (ED) showed very intense spots assignable to α-Fe_2O_3, and this indicated the formation of a highly crystallized α-Fe_2O_3 phase. Because several α-Fe_2O_3 crystals were randomly oriented in different directions, several patterns were mixed with each other. From a high-reso-

Table 2. Mössbauer parameters of samples calcined for 5 and 7 h.

Calcination time [h]	Isomer shift [mm s^{-1}]	Hyperfine field [kOe]	Quadrupole splitting [mm s^{-1}]	FWHM[a] [mm s^{-1}]	Relative peak area [%]	Phase
5	0.37	505.5	–0.22[b]	0.34	23	α-Fe_2O_3
5	0.34	0	0.73	0.56	77	
7	0.37	505.8	–0.23[b]	0.28	64	α-Fe_2O_3
7	0.33	0	0.73	0.57	36	

[a] FWHM = full width at half maximum. [b] $(S_2 - S_1)/2$; S_1 and S_2 are differences of the two outer peaks on the lower and higher velocity side of the sextet, respectively.

lution TEM image, clear lattice fringes were oriented in the same direction at the edge of the cube, which confirmed the formation of the α-Fe_2O_3 crystalline phase (Figure 5, a). The surface area and pore volume were calculated to be 163 $m^2 g^{-1}$ and 0.89 $cm^3 g^{-1}$, respectively, from the corresponding N_2 adsorption–desorption isotherms. These values were much lower than those of the sample that was calcined for 4 h (480 $m^2 g^{-1}$ and 1.5 $cm^3 g^{-1}$, respectively).[23]

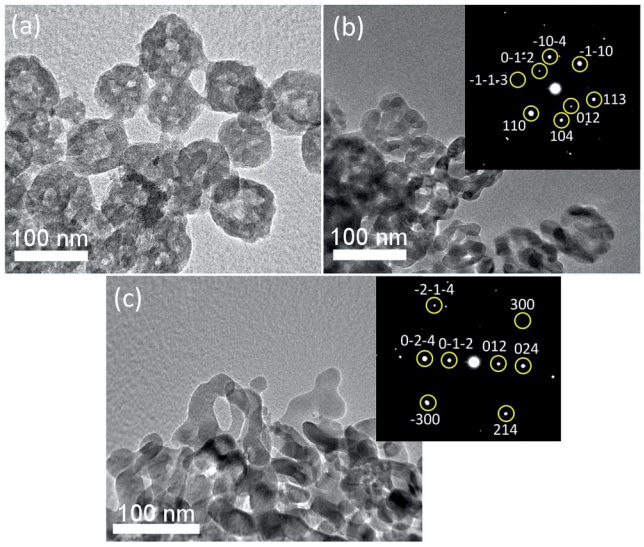

Figure 4. TEM images and the corresponding ED patterns of (a) PB nanoparticles after chemical etching, and samples calcined for (b) 5 and (c) 7 h.

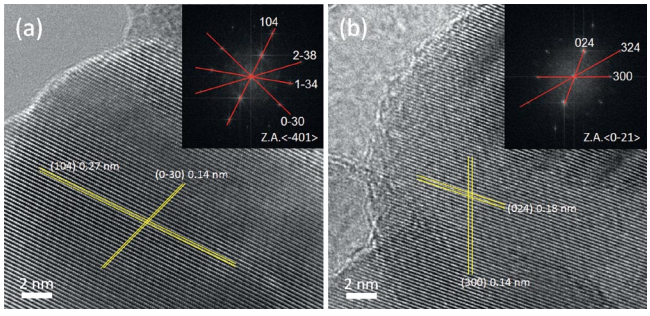

Figure 5. High-resolution TEM images and corresponding fast Fourier transform (FFT) images of samples calcined for (a) 5 and (b) 7 h.

In contrast, long calcination times of 6 and 7 h destroyed the original hollow structures (Figure 4, c). However, a continuous nanoporous structure derived from the original hollow structure was well developed. The surface areas and pore volumes were calculated to be 100 and 0.50 (for 6 h) and 70.0 $m^2 g^{-1}$ and 0.41 $cm^3 g^{-1}$ (for 7 h), respectively. Although a longer calcination time decreased the surface areas of the samples upon crystallization of α-Fe_2O_3, these values are highly relative to those of other nanostructured α-Fe_2O_3 previously reported (Table 1).

Our porous iron oxides with the α-Fe_2O_3 phase are useful as photocatalysts. To investigate the photocatalytic activity, the photocatalyst (5.0 mg, several iron oxide samples calcined for 5, 6, and 7 h) was mixed with methylene blue (MB, 0.01 mM, 15 mL) and then sonicated in a cool water bath for 5 min. Afterward, the suspension was magnetically stirred in the dark for 4 h to reach the complete adsorption–desorption equilibrium, which was followed by the addition of hydrogen peroxide solution (30 wt.-%, 0.2 mL); the bottle was then exposed to UV light irradiation at room temperature.

The time-dependent UV/Vis absorption spectra in the absence and presence of iron oxides are shown in Figure S1 (Supporting Information). The remaining MB concentration was analyzed by measuring the peak intensity derived from MB at 664 nm. With an increase in the irradiation time, the maximum absorption intensity gradually decreased; this suggests the decolorization and decomposition of the MB molecules (Figure S1, Supporting Information). In a control experiment without the photocatalyst, the decomposition rate under UV light was very slow. In the presence of the photocatalyst, the decomposition rate was significantly increased. With an increase in the hematite (α-Fe_2O_3) content (i.e., with an increase in the calcination time), the decomposition rate of the MB molecules increased (Figure 6). The sample calcined for 7 h exhibited the highest decomposition rate of all the samples as a result of the high content of the crystallized hematite phase (α-Fe_2O_3), which was confirmed by Mössbauer spectroscopy (Figure 3). It is suggested that the mechanism for the decomposition of the dye occurs on the photocatalyst surface rather than in the bulk solution. Some electrons generated

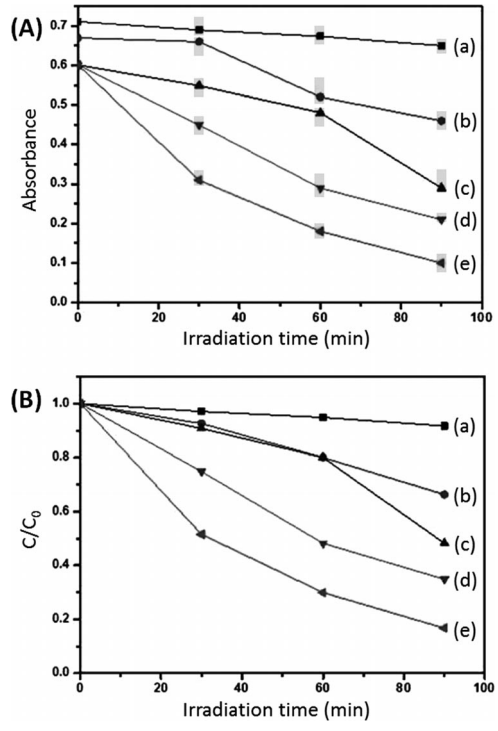

Figure 6. Time-dependent change of (A) absorbance at 664 nm and (B) MB concentration (C_o means the initial MB concentration before UV irradiation): (a) MB (without catalyst), (b) MB and H_2O_2 (without catalyst), and samples calcined for (c) 5, (d) 6, and (e) 7 h. The error bars are also shown in Figure (A).

on the surface under UV light are directly trapped by H_2O_2 to form OH· radicals. As a result, the OH· radicals lead to the photocatalytic reaction.[24]

Conclusions

To conclude, we established a facile route to prepare nanoporous iron oxides with an α-Fe_2O_3 crystalline phase by thermal decomposition of PB coordination polymers. By using hollow PB particles as the starting material, we prepared well-organized nanoporous iron oxides with high surface areas and large pore volumes. Their crystalline phases and degrees were controlled by several calcination conditions. The use of PB as the starting material is a new and unique technology, and further use of various PB analogues with different compositions will produce more functional materials in the future.

Experimental Details

Preparation of Hollow PB Nanoparticles: According to our previous papers,[22,23] PVP (K30, 3.0 g) and $K_3[Fe(CN)_6]\cdot 3H_2O$ (132 mg) were added to 0.01 M HCl (40.0 mL) under magnetic stirring. After 30 min of stirring, a clear solution was obtained. The vial was then placed into an electric oven and heated at 80 °C for 20 h. After aging, the precipitate was collected by centrifugation and washed several times with distilled water and ethanol. After drying at room temperature for 12 h, PB nanocubes of approximately 100 nm in particle size were obtained. For creation of a hollow cavity, PB nanocubes (40.0 mg) and PVP (200 mg) were added to 1.0 M HCl (40 mL) in a Teflon vessel under magnetic stirring. After 2 h, the vessel was transferred into a stainless autoclave and heated at 140 °C for 4 h in an electric oven. After aging, the precipitate was collected by centrifugation and washed with distilled water and ethanol several times. After drying at room temperature for 12 h, hollow PB nanocubes were obtained.

Characterization: SEM images were taken with a Hitachi SU8000 scanning microscope at an accelerating voltage of 5 kV. TEM observation was performed by using a JEM-2100F TEM system that was operated at 200 kV and equipped for energy-dispersive spectrometer analysis. Wide-angle powder XRD patterns were obtained with a Rigaku RINT 2500X diffractometer by using monochromated Cu-K_α radiation (40 kV, 40 mA) at a scanning rate of 2 °min^{-1}. N_2 adsorption–desorption isotherms were measured on a high precision adsorption measuring apparatus BELSORP-mini (BEL Japan) and quanta chrome Autosorb1 Automated Gas Sorption System. Prior to the measurements, the samples were degassed in vacuo. The surface areas were calculated by the BET method by using the adsorption branches of the isotherm. ^{57}Fe Mössbauer spectra were recorded at room temperature in transmission geometry by using a ^{57}Co/Rh γ-ray source. The source velocity was calibrated by using α-Fe as a reference material. TG–DTA–MS were measured with a Rigaku Thermo Mass Photo TG-DTA-PIMS 410/S. The detection range of the MS was from 1 to 250 *m*/*z*. The sample and α-Al_2O_3 standard were separately loaded inside platinum pans, and heated from room temperature to 1000 °C at 10 °Cmin^{-1} under He/O_2 flow to analyze the mass spectrometry of thermally produced compounds.

Supporting Information (see footnote on the first page of this article): Time-dependent UV/Vis spectra.

Acknowledgments

Mr. Natsuhiko Sugimura, Mr. Takahiro Yatsu, and Dr. Takeo Suga (Waseda University, Japan) are acknowledged for kind assistance with the TG-DTA-MS measurements. K. C.-W. W would like to thank the following institutions for funding support: National Science Council of Taiwan (101-2628-E-002-015-MY3), National Taiwan University (102R7842 and 102R7740), Center of Strategic Materials Alliance for Research and Technology (SMART Center), National Taiwan University (102R104100).

[1] B. V. Reddy, S. N. Khanna, *Phys. Rev. Lett.* **2004**, *93*, 068301.
[2] a) P. Poizot, S. Laruelle, S. Grugeon, L. Dupont, J. M. Tarascon, *Nature* **2000**, *407*, 496; b) B. Koo, H. Xiong, M. D. Slater, V. B. Prakapenka, M. Balasubramanian, P. Podsiadlo, C. S. Johnson, T. Rajh, E. V. Shevchenko, *Nano Lett.* **2012**, *12*, 2429.
[3] B. Wang, J. S. Chen, H. B. Wu, Z. Wang, X. W. (D.) Lou, *J. Am. Chem. Soc.* **2011**, *133*, 17146.
[4] X. Yao, C. Tang, G. Yuan, P. Cui, X. Xu, Z. Liu, *Electrochem. Commun.* **2011**, *13*, 1439.
[5] L. S. Zhong, J. S. Hu, H. P. Liang, A. M. Cao, W. G. Song, L. J. Wan, *Adv. Mater.* **2006**, *18*, 2426.
[6] Y. Song, S. Qin, Y. Zhang, W. Gao, J. Liu, *J. Phys. Chem. C* **2010**, *114*, 21158.
[7] A. K. Ganguli, T. Ahmad, *J. Nanosci. Nanotechnol.* **2007**, *7*, 2029.
[8] C. Y. Cummings, F. Marken, L. M. Peter, K. G. Wijayantha, A. A. Tahir, *J. Am. Chem. Soc.* **2012**, *134*, 1228.
[9] X. Gou, G. Wang, X. Kong, D. Wexler, J. Horvat, J. Yang, J. Park, *Chem. Eur. J.* **2008**, *14*, 5996.
[10] L. P. Zhu, H. M. Xiao, X. M. Liu, S. Y. Fu, *J. Mater. Chem.* **2006**, *16*, 1794.
[11] G. Y. Zhang, Y. Feng, Y. Y. Xu, D. Z. Gao, Y. Q. Sun, *Mater. Res. Bull.* **2012**, *47*, 625.
[12] Z. Jia, Q. Wang, D. Ren, R. Zhu, *Appl. Surf. Sci.* **2013**, *264*, 255.
[13] H. C. Liang, Z. H. Ye, S. Z. Yu, L. Z. Min, *Sci. China Chem.* **2010**, *7*, 1502.
[14] S. Bharathi, D. Nataraj, D. Mangalaraj, Y. Masuda, K. Senthil, K. Yong, *J. Phys. D: Appl. Phys.* **2010**, *43*, 015501.
[15] K. Brezesinski, J. Haetge, J. Wang, S. Mascotto, C. Reitz, A. Rein, S. H. Tolbert, J. Perlich, B. Dunn, T. Brezesinski, *Small* **2011**, *7*, 407.
[16] G. Li, M. Liu, H. Z. Kou, *Chem. Eur. J.* **2011**, *17*, 4323.
[17] D. Chen, D. Chen, X. Jiao, Y. Zhao, *J. Mater. Chem.* **2003**, *13*, 2266.
[18] J. Chen, L. Xu, W. Li, X. Gou, *Adv. Mater.* **2005**, *17*, 582.
[19] H. J. Song, N. Li, X. Q. Shen, *Appl. Phys. A: Mater. Sci. Process.* **2011**, *102*, 559.
[20] Z. Wu, K. Yu, S. Zhang, Y. Xie, *J. Phys. Chem. C* **2008**, *112*, 11307.
[21] A. Mitra, C. Vázquez-Vázquez, M. A. López-Quintela, B. K. Paul, A. Bhaumik, *Microporous Mesoporous Mater.* **2010**, *131*, 373.
[22] M. Hu, S. Furukawa, R. Ohtani, H. Sukegawa, Y. Nemoto, J. Reboul, S. Kitagawa, Y. Yamauchi, *Angew. Chem.* **2012**, *124*, 1008; *Angew. Chem. Int. Ed.* **2012**, *51*, 984.
[23] M. Hu, A. A. Belik, M. Imura, K. Mibu, Y. Tsujimoto, Y. Yamauchi, *Chem. Mater.* **2012**, *24*, 2698.
[24] X. Zhou, H. Yang, C. Wang, X. Mao, Y. Wang, Y. Yang, G. Liu, *J. Phys. Chem. C* **2010**, *114*, 17051.

Received: October 6, 2013
Published Online: February 6, 2014

